Photonic candle – focusing light using nano-bore optical fibers

HENRIK SCHNEIDEWIND,[1,*] **MATTHIAS ZEISBERGER,**[1] **MALTE PLIDSCHUN,**[1,2] **STEFAN WEIDLICH,**[1,3] **AND MARKUS A. SCHMIDT**[1,2,4]

[1]*Leibniz Institute of Photonic Technology, Albert-Einstein-Str. 9, 07745 Jena, Germany*
[2]*Abbe Center of Photonics and Faculty of Physics, Friedrich-Schiller-University Jena, Max-Wien-Platz 1 07743, Jena, Germany*
[3]*Heraeus Quarzglas GmbH & Co. KG, Quarzstr. 8 63450, Hanau, Germany*
[4]*Otto Schott Institute of Material Research, Friedrich-Schiller-University Jena, Fraunhoferstr. 6 07743, Jena, Germany*
*henrik.schneidewind@leibniz-ipht.de

Abstract: Focusing light represents one of the fundamental optical functionalities that is used in a countless number of situations. Here we introduce the concept of nano-bore optical fiber mediated light focusing that allows to efficiently focus light at micrometer distance from the fiber end face. Since the focusing effect is provided by the fundamental fiber mode, device implementation is extremely straightforward since no post-processing or nano-structuring is necessary. Far-field measurements on implemented fibers, simulations, and a dual-Gaussian beam toy model confirm the validity of the concept. Due to its unique properties such as strong light localization, a close to 100% implementation success rate, extremely high reproducibility, and its compatibility with current fiber circuitry, the concept will find application in numerous areas that demand to focus at remote distances.

1. Introduction

Focusing light represents one of the basic optical functionalities that is used in a countless number of applications in basic and applied science as well as in industrial and many other applications. Besides the most-well established optical element – the convex dielectric lens – new approaches to focus light have been developed on the basis of planar micro- and nanostructures including geometries such as ultrathin meta-surface lenses and axicons [1–4].

An increasing number of applications demand photonic devices that combine flexible transportation of light over meter to kilometer distances with strong light focusing at the device's end. One of the most efficient ways to deliver light to desired location over such distances is represented by step index optical fibers (SIFs). In this type of waveguide an increased core refractive index (RI) mediates total internal reflection confining propagating light to a micrometer size core. Shaping and functionalizing the end faces of optical fibers with micro- and nano-engineered elements greatly enhance the fiber's functionality, representing one highly addressed scientific objective within fiber optics research, with applications in a multitude of areas including plasmonics [5,6], vector beam generation [7], and sensing (an extensive review of fiber end face structures can be found in [8]). Beside state-of-the-art lithographic approaches such as lithography [9–11] or focused ion beam milling [12,13], extremely promising attempts to implement sophisticated lens designs have recently been conducted on the basis of 3D-nanoprinting [14,15]. For instance Gissibl et al. have shown that two-photon-polymerization-based nano-printing using a Nanoscribe System allows for the implementation of ultra-compact multi-lens objectives on the end face of optical fibers, having opened up new application areas for fiber optics [16]. Other highly

relevant schemes to include sophisticated device functionalities onto fiber end faces include chemical etching [17] and micro-grinding [18].

Any of the mentioned fiber-based devices demand one or more post-processing step (e.g., lithography, etching, or nano-printing) for the actual implementation of the focusing element. Here particular wafer-related technologies are intrinsically incompatible with the cylinder-type fiber geometry, thus imposing strong sample-to-sample variations, low implementation success rate, time-consuming fabrication, complicated and sometimes even manual sample handling, and, most severely, only one or a few devices can be produced at a time.

Kim et al. [19] showed the generation of Bessel beams using hollow core fibers equipped with lenses. Due to the large core diameters (10-30 μm) the field maximum evolves at relatively large distances (> 100 μm) from the fiber end faces.

Here we present the concept of focusing light using nano-bore optical fibers (NBFs) within a region close (e.g. 7 μm) to the end face. This concept is based on a novel type of nanostructured fiber that intrinsically focusses light at micrometer distance from its end face, as illustrated in Fig. 1(b), and does not demand any type of post-processing. The focusing effect is mediated by the fundamental fiber mode, yielding extremely straightforward device implementation at close to 100% success rates: Merely a flat cleave is required to implement the actual device, breaking through all above-mentioned bottlenecks. Both measurements and simulations confirm the observed focusing effect, while a dual Gaussian beam toy model unlocks its underlying physical principles.
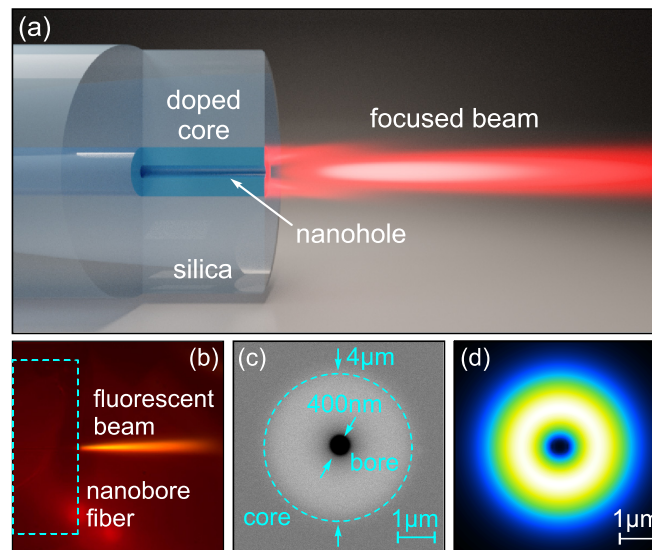

Fig. 1. (a) Illustration of the nano-bore optical fiber mediated focusing effect (red: focused output light, dark blue: doped core with the nano-hole, semitransparent gray: silica cladding). The extension of the output beam shown here is to scale with simulations. (b) Microscopic image of the fluorescence light of the beam that is emitted by the NBF in case the fiber is immersed in Rhodamine 6G doped water (the cyan dashed line indicates the boundary of the NBF). (c) Scanning electron micrograph of the core section of the NBF. The cyan dashed circle indicates the doped core region (diameter $2b = 4$ μm) and the central two arrows the bore (diameter $2a = 400$ nm). (d) Spatial distribution of the intensity (wavelength 650 nm) of the fundamental mode of the NBF shown in (b). The color ranges linearly from 1 (white) to 0 (black).

2. Materials and methods

The fiber geometry used in the present work consists of a cylindrical step index core (radius b, RI n_{co}) embedded in a low RI cladding (RI n_{cl}), as shown schematically in Fig. 1(a). A nano-bore (radius a, RI n_h) that extends through the entire length of the fiber is located

exactly in the center of the structure, which together with the high RI core defines the NBF geometry. In case $n_h < n_{co}$, the fields inside the nano-bore are evanescent and the geometry supports defined optical modes that all, including the fundamental HE_{11} mode, have doughnut-type shapes as shown in Fig. 1(d), which is in contrast to, e.g., the fundamental mode of conventional steps index fibers (field amplitude is finite at zero radial distance) and is essential for the focusing behavior described below.

Within the scope of this work NBFs have been implemented on the basis of drawing silica based preforms containing GeO_2 doped silica cores (core/cladding RI difference $\Delta n = 8 \times 10^{-3}$) and central holes into fiber (core diameter $2b = 4$ μm, outer fiber diameter 200 μm, Fig. 1(c); fabrication details reported in [20]). Several kilometers of NBFs that are single mode at visible wavelengths (the single-mode cut-off wavelength has been measured to be 550 nm using the methods described in [21]) have been realized by drawing a single hole preform, with the drawing conditions adjusted such to reach defined and prechosen bore diameters between $2a = 100$ nm and 800 nm. The result of the fabrication process is a nanostructured optical fiber that contains a step-index core and a longitudinal nano-channel with cross sections that are maintained over hundreds of meters with constant values of a and b. Due to the straightforward fabrication and the precisely controlled fiber dimensions, NBFs have been employed in a series of experiments, including azimuthal mode polarization [22], the implementation of near field tips [23], single nano-object detection [20,24], and in-fiber absorption spectroscopy. It is important to note that other, more complex types of NBF geometries have been implemented on the basis of photonic crystal fibers [25–27], whereas our structure is compatible with fiber circuitry and demands substantially less fabrication efforts. The feature that our NBF only contains one single hole allows avoiding complicated post-processing procedures (e.g., multiple hole blocking) that are sometimes required within the scope of photonic crystal fibers, making the step-index NBF geometry highly attractive for numerous applications.

The actual implementation of the NBF-based focusing device only demands one single cleave, avoiding any kind of post-processing or nano-structuring technique. Here we used a standard cleaving device (Fujikura CT-30 high precision cleaver) or a ceramic tile, instantaneously yielding operating NBF devices at an implementation success rate of close-to 100%.

The experimental characterization of the far-field beam emitted by the NBF has been conducted via scanning near-field optical microscopy (SNOM) in non-contact mode. Here we have chosen SNOM for the spatial characterization since this method gives very high spatial resolution along both longitudinal and spatial directions in order to capture all the fine features of the output field. Specifically, we mounted 1 m long pieces of NBF into a commercially available near field microscope (Nanonics MultiView-4000) operating at a wavelength of $\lambda_0 = 650$ nm and laterally scanned a fiber-based near field tip at a defined height z_0 above the end face of the NBF under investigation to obtain the transverse light distribution. The combination of near field tip (diameter of aperture: 100 nm) and scanning controller yields a transverse spatial resolution of 80 nm (mainly defined by the diameter of the tip aperture), while along the axial direction (along the axis of the NBF fiber) we achieved a resolution of 20 nm (defined by the stepper motor for vertical tip positioning). Efficient excitation of the fundamental NBF mode was provided by launching narrow band light – emitted by a combination of a white light source (NKT Photonics, SuperK Power) and an acousto-optical tunable filter – into the NBF, yielding a fundamental output mode in all situations considered here.

3. Results

In order to simulate the measured far-field properties, we employed a combination of modal calculation and far-field simulation using Finite-Element modelling (Comsol). Specifically the mode profile of the HE_{11} mode of the NBF geometry used here was obtained by a numeric

port in an axially-symmetric model with azimuthal index $m = 1$. The size parameters are depicted in Fig. 1(c). In a second step the field longitudinally propagating away from the port was simulated in a simulation area (15×30) μm^2 in the r-z-plane which was surrounded by perfectly matched layers. We calculated the transverse distribution of the intensity (perpendicular to the fiber axis) at different heights above the NBF surface ($\lambda_0 = 650$ nm) assuming $2a = 0.4$ μm and $2b = 4$ μm and the following RI distribution: $n_{co} = 1.448$, $n_{cl} = 1.440$, $n_h = 1$.

Figure 2(a) shows the measured far-field distributions. They show a strong focusing of the beam exiting the NBF at micrometer distances. We measure a clear evolution of a transverse field pattern that resembles the shape of the fundamental mode at small heights ($z_0 < 2$ μm) as given in Fig. 1(d) towards a Gaussian-type pattern at large heights (e.g., $z_0 > 15$ μm) with the highest local intensity and smallest focal width located at around $z_0 = 7$ μm. A visualization of the focus width is given in Fig. 4(a). This behavior is fully reproduced in simulations showing a "candle"-like intensity distribution along the longitudinal direction according to Fig. 2(b).
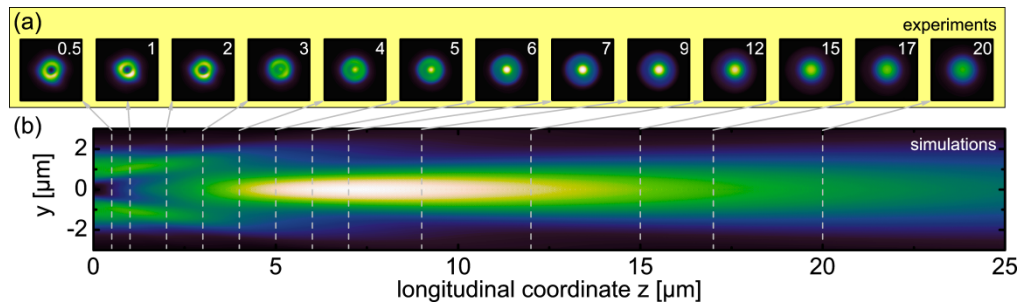

Fig. 2. Qualitative comparison of the measured far-field distributions to simulations. (a) Spatial distribution of the intensity at $\lambda_0 = 650$ nm at various heights above the end-face of the NBF shown in Fig. 1(c) with the distance to fiber surface indicated in each plot by the top right number (in μm). All plots have dimensions of (10×10) μm^2. The color range spans linearly from 0 (black) to 1 (white), whereas all curves have been normalized to the maximum intensity value of the curve referring to $z_0 = 7$ μm. (b) Corresponding simulations showing the intensity distribution (normalized to the maximum value, color range scales linearly from 0 (black) to 1 (white)) along the propagation direction across one arbitrary transverse direction (labeled as y). The vertical dashed gray lines indicate the distance to the NBF surface at which the measurements shown in Fig. 2(a) have been performed.

For $z_0 < 2$ μm the measured far-field distributions show slight deviations from perfect azimuthal symmetry, which we attribute to the interaction of scanning tip and NBF end face. Particular due to the non-ideal shape of the tip, this interaction disturbs the data acquisition process at small values of z_0, with this asymmetry vanishing for sufficient large distances ($z_0 > 3$ μm).

For a qualitative comparison we extracted the intensity distribution of the measured far-field profiles along an arbitrary line that intersects the center of the pattern at different heights and compared these line distributions to corresponding simulations as shown in Fig. 3(a)-3(b). An excellent qualitative agreement is observed particular for $z_0 > 4$ μm, whereas slight deviations emerge for $z_0 < 4$ μm (as previously discussed) which have no visible influence on the actual focusing effect. To demonstrate the impact of the nano-hole we simulated the far-field distribution in absence of the nano-hole as it is shown in Fig. 3(c), i.e., for a regular step index fiber. Neither a focusing effect nor a double-lobe feature is observed at any value of z_0, clearly highlighting the relevance of the nano-hole. For distance $z \geq 9$ μm, the width of the output beam of the NBF increases towards larger distances similar to the behavior of the regular step index fiber, revealing that the presence of the nano-hole has negligible impact on the diffraction of the NBF-beam. A direct qualitative comparison shows that the width of the beam of the NBF is about 8% smaller for $z \geq 9$ μm.

To gain a better understanding of physical origin of the focusing effect we introduce a figure-of-merit (FoM) parameter, which is related to the on-axis surface-peak intensity contrast and is defined as:

$$c = \frac{I_{max} - I_0}{I_{max} + I_0},$$

(1)

with the maximum intensity in the focus spot I_{max} and the intensity at the end of the NBF I_0, both at $r = 0$. In case of a well-defined focusing spot, the FoM parameter approaches unity, while weak focusing leads to small values, making it possible to compare different NBF and environmental configurations. Figure 4(b) shows the simulated dependence of the intensity contrast c corresponding to Eq. (1) as a function of bore diameter for three different bore and environment refractive indices at two wavelengths, clearly showing that (i) larger bore diameters lead to a more pronounced focusing effect, (ii) focusing is observed both wavelengths considered, and (iii) the presented concept of light focusing using NBF also works in case the fiber is filled with water or another liquid in case an sufficiently large bore diameter is chosen, making our concept particular suitable for bioanalytical applications.
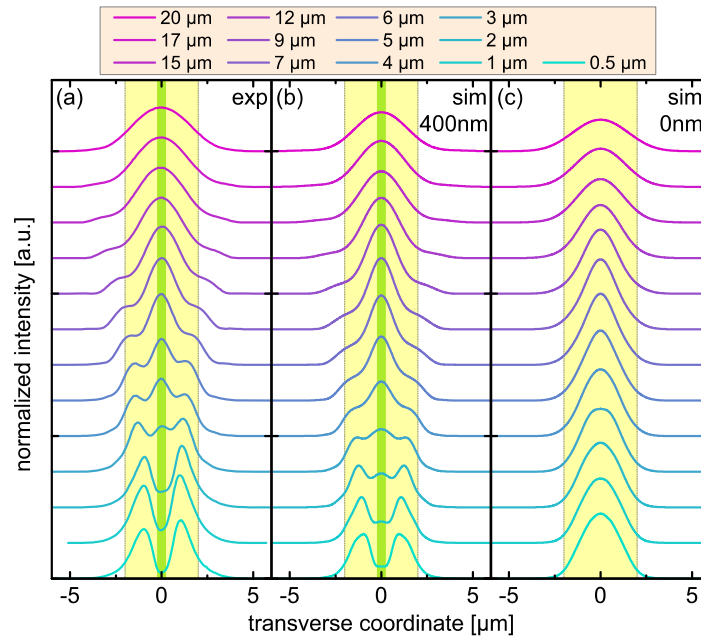

Fig. 3. Quantitative comparison of (a) measured and (b) simulated spatial intensity distributions, both along one arbitrarily chosen transverse line through the center of the respective plot at various heights above the NBF end-face (each of the colored lines refers to a different distance (given in the top legend), $2a = 400$ nm). The yellow backgrounds indicate the doped core regions, the light green the domains of the nano-hole. (c) Simulations of a fiber that includes no nano-hole (i.e., a regular step index geometry) while all other parameters are identical to the NBF are presented in Fig. 1(c). All plots refer to a wavelength of 650 nm.

In addition we also simulated various lens-related parameters (focus depth, position, and width, respectively) as function of bore diameter while keeping all other parameters constant ($\lambda_0 = 650$ nm, $n_h = 1$; the focal depth was defined here as the FWHM of the axial intensity distribution). The results are given in Fig. 4(c). The overall dependence of these parameters on bore diameter is comparably weak. A slight increase of focus position and depth towards larger bore diameters is observed, which is in qualitative correspondence with the toy model presented in the subsequent section. It is important to note that the curves presented in the

inset of Fig. 4(b) suggest the impact of the nano-hole being more relevant for the side of the focus that points towards the fiber end face ($z \lesssim 10$ μm) than for the opposite side ($z \gtrsim 10$ μm). Please note that the intensity distribution observed here arises from the diffraction of a ring shaped light source. Therefore the beam of our system is not a Bessel beam since we do not use an axicon to induce a radial phase variation, which is in contrast to the configuration discussed in [19].
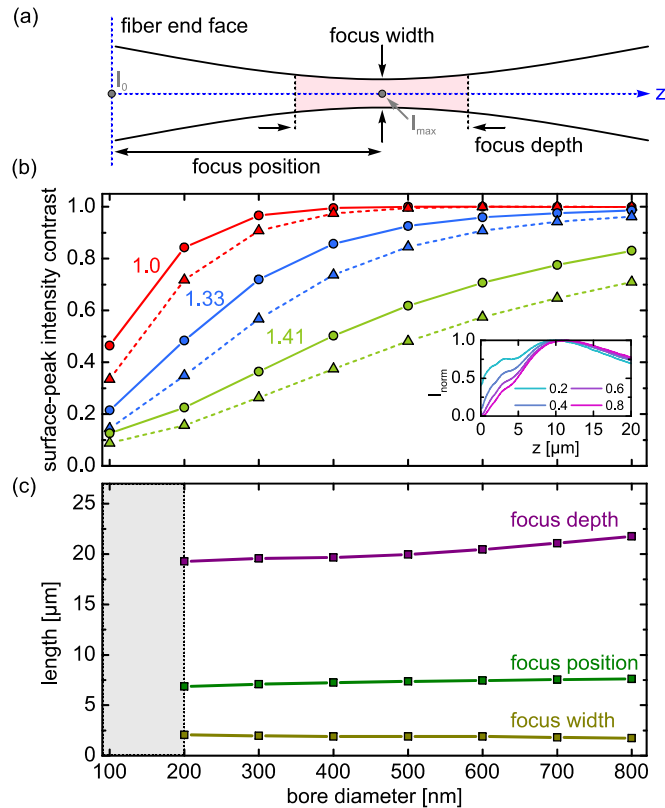

Fig. 4. Dependence of various lens-related parameters on the diameter of the nano-hole (simulation assume the NBF discussed in Fig. 3). (a) Sketch of a focused beam including the parameters discussed in the subsequent plots. The light red region indicates the domain of the focus. (b) On-axis surface-peak intensity contrast ($r = 0$) as function of bore diameter for three different bore and environment refractive indices at two different wavelengths (red: $n_h = 1$ (air), blue: $n_h = 1.33$ (water), light green: $n_h = 1.41$ (high index liquid)). The circles and triangles refer to a wavelength of 532 nm and 650 nm, respectively (the lines are guide-to-the-eyes). The inset exemplarily shows the spatial on-axis intensity distribution for four different nano-bore diameters normalized to the maximum intensity of the respective curve (numbers in the legend refer to the bore diameter in units of μm, $\lambda_0 = 532$ nm, $n_h = 1.33$). (c) Focus depth (purple), focus position (green) and focus width (dark yellow) as function of bore diameter ($\lambda_0 = 650$ nm, $n_h = 1$). Within the gray region (bore diameter < 200 nm), determining the lens-related parameters was not possible due to weak focusing.

To understand the physics of the focus spot formation provided by the NBF geometry more clearly, we present the results of qualitative toy model as sketched in Fig. 5(a) assuming the interference of two identical fundamental Gaussian beams (GBs, characterized by beam waist parameter w_0) that are separated by a defined lateral distance perpendicular to the emission direction (edge-to-edge distance Δ). This arrangement resembles to a certain degree the situation of the NBF cross section along the radial coordinate, which is assumed within the toy model to be composed of two single mode waveguides (WGs) which emit their

individual Gaussian beam with zero relative phase. The on-axis intensity distribution (along the symmetry axis (z-axis), dashed blue line in Fig. 5(a), $r = 0$) can be straightforwardly calculated by the sum of the electric field of the two Gaussian modes considered yielding (see Appendix for details) as:

$$I_s(z) = 4\left(\frac{w_0}{w(z)}\right)^2 \exp\left(-\frac{d^2}{2w(z)^2}\right),\qquad(2)$$

with the radial and longitudinal coordinates r and z, respectively, the local beam width:

$$w(z) = w_0\sqrt{1+\left(\frac{z}{z_R}\right)^2},\qquad(3)$$

and the Rayleigh length $z_R = n_h \pi w_0^2 / \lambda_0$. It is interesting to note that Eq. (2) neither includes the radius of the beam's wave front nor the Gouy phase, with the only relevant parameters being the inter-WG distance and the beam waist. Please note that the refractive index of the medium surrounding the NBF and the wavelength enter Eq. (2) only via the Rayleigh length, while all other parameters remain unaffected. This allows a change of the refractive index to be compensated by an appropriate choice of wavelength. The situation of the NBF addressed
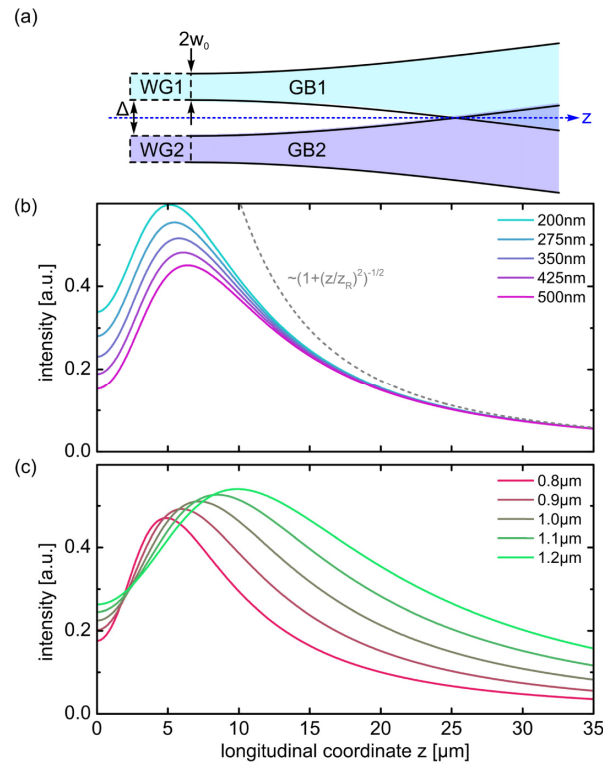

Fig. 5. Dual-Gaussian beam based toy model resembling the NBF geometry along one transverse line of the fiber cross section. (a) Sketch of two Gaussian beams (GBs) that are emitted by two identical waveguides (WGs) spaced apart by a distance Δ, and interfere after a certain distance. The parameters are defined in the text. (b) On-axis intensity distribution (at $r = 0$) as function of longitudinal coordinate z for different WG separation distances Δ (defined in the legend; $w_0 = 2$ µm). The grey dashed curve refers to the left-handed term of the right side of Eq. (2). (c) Dependence of on-axis intensity on axial coordinate for different values of beam waist parameter w_0 (defined by the legend) assuming $\Delta = 0.4$ µm.

in this work is geometrically considered when assuming $w_0 = (b-a)/2$ and $\Delta = 2a$. An intuitive interpretation of Eq. (2) is that it represents the intensity of a Gauss beam along a line parallel to the axis with distance d.

Simulations of the spatial distribution of the on-axis intensity distribution, which are given in Figs. 5(b)-5(c), show a qualitatively similar behavior to that of the NBF (compare Fig. 2(a) and inset of Fig. 4(b)), i.e., an increase of IS from a finite value at z = 0 to a maximum, followed by a decrease. The intensity decrease on the right side of the peak (z > 6 μm) shows an overall smaller slope compared to the decay towards small z (left side of the peak). A detailed investigation of the intensity distribution for different values of Δ as shown in Fig. 5(b) reveals that this behavior can be explained by the two factors of Eq. (2): On the left side of the peak (z < 6 μm), the increase of IS is governed by the exponential factor, whereas for z > 6 μm the decay is dominated by the first factor being proportional to $1/\sqrt{1+(z/z_R)^2}$ (dashed grey curve in Fig. 5(b)). The latter dependency has clear implications for the observed focusing effect, since the WG separation distance Δ is only relevant for the initial increase, whereas the intensity decay for z > 6 μm is solely dominated by w0 which is correlated with the properties of the WGs used. Therefore the model suggests that a faster intensity reduction on the right side of the peak requires reducing the Rayleigh length, i.e., w0, implying to use NBFs with large RI contrast such as micro-structured suspended core fibers or photonic crystal fibers made from glasses with high refractive index [27]. This finding is qualitatively confirmed in Fig. 5(c) showing that the tail of IS(z) extends towards large longitudinal coordinates when increasing w0 (Δ = 400 nm), i.e., assuming more weakly confining WGs. The intensity at the end of the two WGs (z = 0) is given within the scope of the toy model by:

$$I_S^0 = 4\exp\left(-\frac{1}{2}\left(\frac{\Delta}{w_0}+2\right)^2\right), \tag{4}$$

suggesting that using NBFs with larger bores yield higher intensity contrasts as confirmed in Fig. 4(b).

4. Discussion and applications

Due to its unique properties and in particular the straightforward implementation scheme, the concept of focusing light using NBF is highly attractive for any application that demands remote light delivery/collection and focusing. Please also note that since only cleaving is needed, a NBF-focusing device can in fact be established in any kind of laboratory that has a minimum of optical fiber equipment, while post-processing demands involving infrastructure that is only available in specific places and that is sometimes harmful (e.g., HF-etching in case of silica). Since the simulations show that the focusing effect is hardly impacted in case the bore is filled with water, potential examples of application include integration of NBFs into microfluidic circuits to excite fluorescent species at a defined distance inside small volumes or to efficiently collect light emitted by isolated biologically relevant objects. The concept can also be applied to improve coupling into small core WGs and optical fiber, to implement dual-fiber traps with improved trap stiffness or to establish small mode volume Fabry-Perot resonators. It is important to note that since no additional materials or structures at the NBF end face are required, power damage threshold are as high as for regular silica fibers, suggesting application of the NBF concept in material analysis and processing.

As shown multiple times by the authors [28–30], pressure-assisted melt filling allows placing metals into the bore, with the consequence that the evanescent field inside the hole practically reduces to zero, improving the focus spot intensity enhancement to its maximal possible value while, however, device fabrication is more complex due to an additional post-processing step to fill the NBF, a more difficult cleaving procedure and samples with reduced

mechanical stability. As suggested by the toy model improving the focusing properties at the tail side of the focus spot will require drawing small-core NBFs ideally made from a high RI material. Even though the fabrication of micro-structured soft glass fibers is considerably more challenging than for their silica-based counterparts, recent advancement suggest that the integration of micro- and nano-holes into soft glass step-index fibers is possible [31] particular since geometries with substantially higher complexities, such as the suspended [32–35] or exposed core fibers [36] or hollow core fibers [37,38] have been experimentally realized.

5. Conclusion

Focusing light represents one of the fundamental optical functionalities that is used in a countless number of situations, while many applications demand combining the focusing effect with flexible light transportation over long distances. Here we introduce the concept of focusing light using nano-bore optical fibers, allowing to efficiently focus light at micrometer distance from the fiber end face without using any type of post-processing (i.e., implementation only requires one single cleave). Since the focusing effect is mediated by the fundamental doughnut-shaped fiber mode, device implementation is extremely straightforward at close to 100% success rates as only a flat cleave is required. Far-field measurements conducted on silica-based step index fibers that contain a central nano-channel clearly confirm the validity the concept, with corresponding numerical simulation matching the experiments. A developed toy model that is based on interfering two laterally separated Gaussian beams unlocks the fundamental dependencies and potential pathways for further improvements.

Due to its unique properties such as strong light localization at micrometer distances from the fiber end face, an extraordinary high implementation success rate, extremely high reproducibility, no need for any type of post processing, damage thresholds that are presumably comparable to silica fibers, and its compatibility with current fiber circuitry, the nano-bore fiber mediated light focusing concept will find application in numerous areas including optical trapping, bioanalytics, material science, quantum technology, and any application that demands to focus at remote distances.

Appendix

Superposition of Gaussian modes

The toy model used to describe the focussing behaviour of the nano-bore optical fiber relies on the superposition of two Gaussian beams laterally spaced apart by the edge-to-edge distance Δ. The electric field of the individual Gaussian mode (modal amplitude has been set to unity for convenience) which is a solution of the paraxial Helmholtz Equation and is mainly characterized by the beam waist w_0 is given by:

$$E_G(r,z) = \frac{w_0}{w(z)} \exp\left[-\left(\frac{r}{w(z)}\right)^2\right] \exp\left[-i\left(k_0 z + \frac{k_0 r^2}{2R(z)} + \psi(z)\right)\right],$$

with the radial and longitudinal coordinates r and z, respectively, the local beam width:

$$w(z) = w_0 \sqrt{1+\left(\frac{z}{z_R}\right)^2},$$

the Rayleigh length $z_R = \pi w_0^2 / \lambda_0$, the vacuum vector k_0, the vacuum wavelength λ_0, the radius of curvature of the beam's wavefronts $R(z) = z(1+(z_R/r)^2$, and the Gouy phase $\psi(z) = \arctan(z/z_R)$.

The spatial distribution of the intensity along the central symmetry axis is then given by the superposition of the two electric fields:

$$I_s(z) = \left| E_G\left(r = -\frac{\Delta}{2} - w_0, z \right) + E_G\left(r = \frac{\Delta}{2} + w_0, z \right) \right|^2,$$

yielding Eq. (2) shown in the main text.

Funding

Disclosures

The authors declare that there are no conflicts related to this article.

References

1. N. Yu and F. Capasso, "Flat optics with designer metasurfaces," Nat. Mater. **13**(2), 139–150 (2014).
2. W. T. Chen, A. Y. Zhu, V. Sanjeev, M. Khorasaninejad, Z. Shi, E. Lee, and F. Capasso, "A broadband achromatic metalens for focusing and imaging in the visible," Nat. Nanotechnol. **13**(3), 220–226 (2018).
3. F. Aieta, P. Genevet, M. A. Kats, N. Yu, R. Blanchard, Z. Gaburro, and F. Capasso, "Aberration-free ultrathin flat lenses and axicons at telecom wavelengths based on plasmonic metasurfaces," Nano Lett. **12**(9), 4932–4936 (2012).
4. X. Chen, L. Huang, H. Mühlenbernd, G. Li, B. Bai, Q. Tan, G. Jin, C.-W. Qiu, S. Zhang, and T. Zentgraf, "Dual-polarity plasmonic metalens for visible light," Nat. Commun. **3**(1), 1198 (2012).
5. S. Kang, H.-E. Joe, J. Kim, Y. Jeong, B.-K. Min, and K. Oh, "Subwavelength plasmonic lens patterned on a composite optical fiber facet for quasi-one-dimensional Bessel beam generation," Appl. Phys. Lett. **98**(24), 241103 (2011).
6. A. Tuniz and M. A. Schmidt, "Interfacing optical fibers with plasmonic nanoconcentrators," Nanophotonics **7**(7), 1279–1298 (2018).
7. C. Weibin, H. Wei, C. A. Don, L. N. Robert, and Z. Qiwen, "Generating cylindrical vector beams with subwavelength concentric metallic gratings fabricated on optical fibers," J Opt. **13**(1), 015003 (2011).
8. G. Kostovski, P. R. Stoddart, and A. Mitchell, "The optical fiber tip: an inherently light-coupled microscopic platform for micro- and nanotechnologies," Adv. Mater. **26**(23), 3798–3820 (2014).
9. E. J. Smythe, M. D. Dickey, J. Bao, G. M. Whitesides, and F. Capasso, "Optical antenna arrays on a fiber facet for in situ surface-enhanced Raman scattering detection," Nano Lett. **9**(3), 1132–1138 (2009).
10. X. Yang, N. Ileri, C. C. Larson, T. C. Carlson, J. A. Britten, A. S. P. Chang, C. Gu, and T. C. Bond, "Nanopillar array on a fiber facet for highly sensitive surface-enhanced Raman scattering," Opt. Express **20**(22), 24819–24826 (2012).
11. M. Sasaki, T. Ando, S. Nogawa, and K. Hane, "Direct photolithography on optical fiber end," Jpn. J. Appl. Phys. **41**(1), 4350–4355 (2002).
12. A. Koshelev, G. Calafiore, C. Piña-Hernandez, F. I. Allen, S. Dhuey, S. Sassolini, E. Wong, P. Lum, K. Munechika, and S. Cabrini, "High refractive index Fresnel lens on a fiber fabricated by nanoimprint lithography for immersion applications," Opt. Lett. **41**(15), 3423–3426 (2016).
13. V. Callegari, D. Iwaniuk, R. Bronnimann, E. Schmid, and U. Sennhauser, "Optimized fabrication of curved surfaces by a FIB for direct focusing with glass fibres," J. Micromech. Microeng. **19**(10), 107003 (2009).
14. T. Gissibl, S. Thiele, A. Herkommer, and H. Giessen, "Sub-micrometre accurate free-form optics by three-dimensional printing on single-mode fibres," Nat. Commun. **7**, 11763 (2016).
15. T. Gissibl, M. Schmid, and H. Giessen, "Spatial beam intensity shaping using phase masks on single-mode optical fibers fabricated by femtosecond direct laser writing," Optica **3**(4), 448–451 (2016).
16. T. Gissibl, S. Thiele, A. Herkommer, and H. Giessen, "Two-photon direct laser writing of ultracompact multi-lens objectives," Nat. Photonics **10**(8), 554–560 (2016).
17. A. Kuchmizhak, S. Gurbatov, A. Nepomniaschii, O. Vitrik, and Y. Kulchin, "High-quality fiber microaxicons fabricated by a modified chemical etching method for laser focusing and generation of Bessel-like beams," Appl. Opt. **53**(5), 937–943 (2014).
18. S. Yakunin and J. Heitz, "Microgrinding of lensed fibers by means of a scanning-probe microscope setup," Appl. Opt. **48**(32), 6172–6177 (2009).
19. J. K. Kim, J. Kim, Y. Jung, W. Ha, Y. S. Jeong, S. Lee, A. Tünnermann, and K. Oh, "Compact all-fiber Bessel beam generator based on hollow optical fiber combined with a hybrid polymer fiber lens," Opt. Lett. **34**(19), 2973–2975 (2009).

20. S. Faez, Y. Lahini, S. Weidlich, R. F. Garmann, K. Wondraczek, M. Zeisberger, M. A. Schmidt, M. Orrit, and V. N. Manoharan, "Fast, label-free tracking of single viruses and weakly scattering nanoparticles in a nanofluidic optical fiber," ACS Nano **9**(12), 12349–12357 (2015).

21. K. Schaarschmidt, S. Weidlich, D. Reul, and M. A. Schmidt, "Bending losses and modal properties of nano-bore optical fibers," Opt. Lett. **43**(17), 4192–4195 (2018).

22. A. Tuniz, C. Jain, S. Weidlich, and M. A. Schmidt, "Broadband azimuthal polarization conversion using gold nanowire enhanced step-index fiber," Opt. Lett. **41**(3), 448–451 (2016).

23. A. Tuniz, M. Chemnitz, J. Dellith, S. Weidlich, and M. A. Schmidt, "Hybrid-Mode-Assisted Long-Distance Excitation of Short-Range Surface Plasmons in a Nanotip-Enhanced Step-Index Fiber," Nano Lett. **17**(2), 631–637 (2017).

24. S. Faez, S. Samin, D. Baasanjav, S. Weidlich, M. Schmidt, and A. P. Mosk, "Nanocapillary electrokinetic tracking for monitoring charge fluctuations on a single nanoparticle," Faraday Discuss. **193**, 447–458 (2016).

25. T. G. Euser, M. A. Schmidt, N. Y. Joly, C. Gabriel, C. Marquardt, L. Y. Zang, M. Fortsch, P. Banzer, A. Brenn, D. Elser, M. Scharrer, G. Leuchs, and P. S. Russell, "Birefringence and dispersion of cylindrically polarized modes in nanobore photonic crystal fiber," J. Opt. Soc. Am. B **28**(1), 193–198 (2011).

26. G. S. Wiederhecker, C. M. B. Cordeiro, F. Couny, F. Benabid, S. A. Maier, J. C. Knight, C. H. B. Cruz, and H. L. Fragnito, "Field enhancement within an optical fibre with a subwavelength air core," Nat. Photonics **1**(2), 115–118 (2007).

27. P. Uebel, M. A. Schmidt, M. Scharrer, and P. S. Russell, "An azimuthally polarizing photonic crystal fibre with a central gold nanowire," New J. Phys. **13**(6), 063016 (2011).

28. H. W. Lee, M. A. Schmidt, R. F. Russell, N. Y. Joly, H. K. Tyagi, P. Uebel, and P. S. J. Russell, "Pressure-assisted melt-filling and optical characterization of Au nano-wires in microstructured fibers," Opt. Express **19**(13), 12180–12189 (2011).

29. M. A. Schmidt, L. N. Prill Sempere, H. K. Tyagi, C. G. Poulton, and P. S. J. Russell, "Waveguiding and plasmon resonances in two-dimensional photonic lattices of gold and silver nanowires," Phys. Rev. B Condens. Matter Mater. Phys. **77**(3), 033417 (2008).

30. C. Jain, A. Tuniz, K. Reuther, T. Wieduwilt, M. Rettenmayr, and M. A. Schmidt, "Micron-sized gold-nickel alloy wire integrated silica optical fibers," Opt. Mater. Express **6**(6), 1790–1799 (2016).

31. Y. Ruan, H. Ebendorff-Heidepriem, S. Afshar, and T. M. Monro, "Light confinement within nanoholes in nanostructured optical fibers," Opt. Express **18**(25), 26018–26026 (2010).

32. M. Belal, L. Xu, P. Horak, L. Shen, X. Feng, M. Ettabib, D. J. Richardson, P. Petropoulos, and J. H. V. Price, "Mid-infrared supercontinuum generation in suspended core tellurite microstructured optical fibers," Opt. Lett. **40**(10), 2237–2240 (2015).

33. W. Gao, M. El Amraoui, M. Liao, H. Kawashima, Z. Duan, D. Deng, T. Cheng, T. Suzuki, Y. Messaddeq, and Y. Ohishi, "Mid-infrared supercontinuum generation in a suspended-core As2S3 chalcogenide microstructured optical fiber," Opt. Express **21**(8), 9573–9583 (2013).

34. I. Savelli, O. Mouawad, J. Fatome, B. Kibler, F. Désévédavy, G. Gadret, J. C. Jules, P. Y. Bony, H. Kawashima, W. Gao, T. Kohoutek, T. Suzuki, Y. Ohishi, and F. Smektala, "Mid-infrared 2000-nm bandwidth supercontinuum generation in suspended-core microstructured sulfide and tellurite optical fibers," Opt. Express **20**(24), 27083–27093 (2012).

35. F. Désévédavy, G. Renversez, L. Brilland, P. Houizot, J. Troles, Q. Coulombier, F. Smektala, N. Traynor, and J.-L. Adam, "Small-core chalcogenide microstructured fibers for the infrared," Appl. Opt. **47**(32), 6014–6021 (2008).

36. J. Troles, P. Toupin, L. Brilland, C. Boussard-Plédel, B. Bureau, S. Cui, D. Mechin, and J.-L. Adam, "Exposed-core chalcogenide microstructured optical fibers for chemical sensing," in SPIE Optics+Optoelectronics (SPIE, 2013), p. 5.

37. A. M. Cubillas, X. Jiang, T. G. Euser, N. Taccardi, B. J. M. Etzold, P. Wasserscheid, and P. S. J. Russell, "Photochemistry in a soft-glass single-ring hollow-core photonic crystal fibre," Analyst **142**(6), 925–929 (2017).

38. L. Melnikov, I. Khromova, A. Scherbakov, and N. Nikishin, "Soft-glass hollow-core photonic crystal fibers," in Congress on Optics and Optoelectronics (SPIE, 2005), p. 9.